RSC Advances

PAPER

View Article Online
View Journal | View Issue

Cite this: *RSC Adv.*, 2022, **12**, 32803

Highly porous gold supraparticles as surface-enhanced Raman spectroscopy (SERS) substrates for sensitive detection of environmental contaminants†

Seju Kang, *[ab] Wei Wang, [ab] Asifur Rahman, [ab] Wonil Nam, [cd] Wei Zhou [c] and Peter J. Vikesland *[ab]

Surface-enhanced Raman spectroscopy (SERS) has great potential as an analytical technique for environmental analyses. In this study, we fabricated highly porous gold (Au) supraparticles (*i.e.*, ~100 μm diameter agglomerates of primary nano-sized particles) and evaluated their applicability as SERS substrates for the sensitive detection of environmental contaminants. Facile supraparticle fabrication was achieved by evaporating a droplet containing an Au and polystyrene (PS) nanoparticle mixture on a superamphiphobic nanofilament substrate. Porous Au supraparticles were obtained through the removal of the PS phase by calcination at 500 °C. The porosity of the Au supraparticles was readily adjusted by varying the volumetric ratios of Au and PS nanoparticles. Six environmental contaminants (malachite green isothiocyanate, rhodamine B, benzenethiol, atrazine, adenine, and gene segment) were successfully adsorbed to the porous Au supraparticles, and their distinct SERS spectra were obtained. The observed linear dependence of the characteristic Raman peak intensity for each environmental contaminant on its aqueous concentration reveals the quantitative SERS detection capability by porous Au supraparticles. The limit of detection (LOD) for the six environmental contaminants ranged from ~10 nM to ~10 μM, which depends on analyte affinity to the porous Au supraparticles and analyte intrinsic Raman cross-sections. The porous Au supraparticles enabled multiplex SERS detection and maintained comparable SERS detection sensitivity in wastewater influent. Overall, we envision that the Au supraparticles can potentially serve as practical and sensitive SERS devices for environmental analysis applications.

Received 5th October 2022
Accepted 9th November 2022

DOI: 10.1039/d2ra06248h

rsc.li/rsc-advances

Introduction

Rapid, reliable detection of environmental contaminants is critical for minimizing public health risks that may arise through environmental exposures. Many analytical techniques have been developed to detect environmental contaminants, such as mass spectrometry, liquid/gas chromatography, and polymerase chain reaction (PCR) based biomolecular approaches.[1–4] Although these methods are widely accepted for environmental sensing, there are still certain limitations. The major challenge of conventional analytical techniques is that most require expensive centralized facilities and professional expertise. Additionally, there is the need for environmental samples to be processed appropriately to be analyzed by such sophisticated analytical instruments (*e.g.*, filtration, extraction, and purification), which comes with arduous labor and material costs.[5,6] These challenges can be a bottleneck for environmental analyses in resource-restrained areas (*e.g.*, rural areas, low- and middle-income countries). In this context, the development of sensitive and rapid analytical techniques for detecting environmental contaminants at a low cost is highly desirable.

Surface-enhanced Raman spectroscopy (SERS) has shown its potential as an analytical technique with numerous applications in the environmental sector.[7–14] Inelastic Raman scattering reflects the unique fingerprint of analytes that arise from the vibrational modes of analyte chemical bonds. SERS is the phenomenon whereby the Raman signal of an analyte is significantly enhanced by a factor of 10^5 to 10^6 when it is

[a]*Department of Civil and Environmental Engineering, Virginia Tech, 415 Durham, Blacksburg 24061, Virginia, USA. E-mail: seju@vt.edu; pvikes@vt.edu*
[b]*Virginia Tech Institute of Critical Technology and Applied Science (ICTAS) Sustainable Nanotechnology Center (VTSuN), Blacksburg, Virginia, USA*
[c]*Department of Electrical and Computer Engineering, Virginia Tech, 415 Durham, Blacksburg 24061, Virginia, USA*
[d]*Department of Electronic Engineering, Pukyong National University, Busan, Republic of Korea*

† Electronic supplementary information (ESI) available: Sorption kinetics of environmental contaminants; gene sequences for 498 *int*I1; SERS peaks and corresponding assignments; the composition of wastewater influent. See DOI: https://doi.org/10.1039/d2ra06248h

situated adjacent to the surface of a plasmonic metal substrate.[15] It has been found that the localized surface plasmon resonance (LSPR) of plasmonic nanomaterials provides a near-surface enhanced electromagnetic (EM) field where the Raman signal of an analyte is significantly enhanced, this process results in "SERS hotspots". Achieving high SERS detection sensitivity requires fabrication of SERS substrates with a high hotspot density. In prior studies, colloidal gold (Au) nanoparticles have been used as precursors to create SERS substrates owing to their high SERS enhancement and their stability.[16] Many studies have shown that Au nanoparticle aggregation can lead to dense SERS hotspots.[17–19] However, it remains a challenge to control the extent of aggregation and the association of target molecules with SERS hotspots which in turn influence the SERS spectrum and its intensity.[20–22]

Recently, supraparticles have attracted attention in many areas of science and technology due to their potential role in drug deployment, catalysis, energy production, and storage materials.[23] Supraparticles are agglomerates of primary micro- or nano-sized particles with average sizes in the 10 to 100 μm range. Solid-state supraparticles provide the benefits of facile handling and recovery in aqueous environments. Additionally, using supraparticles can minimize the potential release of nanoparticles into environmental systems. In this context, Au supraparticles as SERS substrates are expected to be advantageous. Au supraparticles not only readily provide dense SERS hotspots due to agglomeration of Au nanoparticles but can also be easily transferred into and out of environmental samples owing to their large size and solid state. Furthermore, the porous structure provides a large surface area, facilitating guest molecule association with the plasmonic nanoparticle surface. A porous Au supraparticle is expected to have SERS hotspots that are highly accessible to guest molecules, thus enhancing sensitivity.[24]

Herein, we developed a highly porous Au supraparticle for sensitive SERS detection of environmental contaminants. Binary supraparticles were fabricated by evaporating an Au and polystyrene (PS) nanoparticle mixture on a superamphiphobic liquid-repellent nanofilament substrate. Then, porous Au supraparticles were made by removing the PS phase from the binary supraparticles through calcination.[25] The porous Au supraparticles were evaluated as SERS substrates for sensitive detection of six different environmental contaminants. In addition, their multiplex capability and applicability in an environmental matrix were investigated.

Materials and methods

Materials

All chemicals used in this study were ACS reagent or molecular biology grade. Malachite green isothiocyanate (MGITC) was purchased from Invitrogen Corp. (Grand Island, NY). Nitric acid (HNO_3), hydrochloric acid (HCl), sodium citrate tribasic dihydrate (Na_3Cit), hydrogen tetrachloroaurate hydrate ($HAuCl_4$), trichloromethylsaline (TCMS), 1*H*,1*H*,2*H*,2*H*-perfluorodecyltrichlorosilane (PFDTS), latex beads (PS nanoparticles; 600 nm mean particle size), rhodamine B (RhoB), benzenethiol (BZT), atrazine (ATZ), adenine, hexane, and toluene were purchased from Sigma-Aldrich (St Louis, MO) or Fisher Scientific (Hampton, NH). A gene segment with an 86-base length was purchased from Integrated DNA Technologies Corp. (Coralville, IA) with the request of polyacrylamide gel electrophoresis (PAGE) purification. Prior to use, all glassware was washed with *aqua regia* – 3 : 1 (v : v) HCl : HNO_3. Nano-pure water (>18.2 MΩ cm) was used as a solvent for solution preparation unless otherwise noted.

Fabrication of superamphiphobic substrates

Fig. 1A illustrates the fabrication of a superamphiphobic substrate following the prior literature with minor revision.[25] A 100 mm diameter silicon wafer was cleaned with toluene, acetone, and ethanol to remove contaminants from the surface, followed by gentle nitrogen flow drying. Then, the wafer was treated with a 30 W oxygen plasma for 2 min. The wafer was incubated in a polypropylene (PP) disposable beaker containing 5 mL of toluene with 3.5 μL of TCMS for 12 h while sealed with PTFE paper. Following incubation, the substrate was rinsed with hexane and dried under nitrogen. The wafer was further treated with a 120 W oxygen plasma for 2 min and incubated in a PP disposable beaker with 5 mL of hexane with 7.5 μL of PFDTS for 30 min while sealed with PTFE paper. Then, the substrate was rinsed again with hexane and dried under

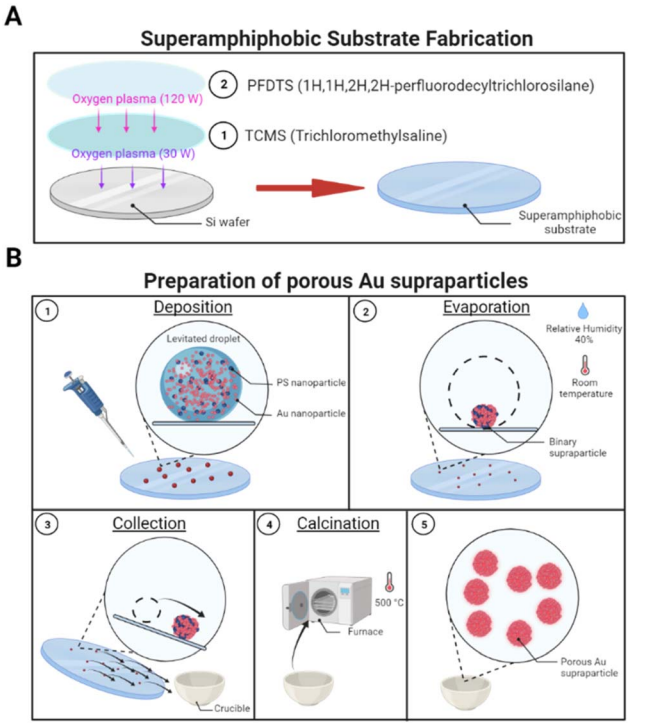

Fig. 1 (A) Fabrication of the superamphiphobic substrate. (B) Preparation of highly porous Au supraparticles. Deposition of a levitated droplet containing Au and polystyrene (PS) nanoparticle mixture on the surface of the superamphiphobic substrates followed by evaporation in a controlled humidity chamber. After evaporation, the binary Au/PS supraparticles were collected by slightly tilting the substrate and then were calcinated in a muffle furnace at 500 °C to produce porous Au supraparticles.

nitrogen. In doing so, the silicon wafer surface was expected to have nanofilaments coated with fluorinated carbons which made it super-liquid repellent. Such surface induced complete pin-free droplet evaporation, resulting in supraparticle fabrication.

Preparation of porous gold supraparticles

Citrate-coated Au nanoparticles were synthesized using the seed-mediated growth method.[26,27] Au seed particles ($\approx$ 13 nm) were made by boiling 100 mL of 1 mM $HAuCl_4$ and 3.88 mM Na_3Cit in a round-bottom flask on a heating mantle while refluxing for 30 min. To synthesize larger-sized Au nanoparticles, we mixed 818 μL of Au seed particles into 100 mL of 0.254 mM $HAuCl_4$ and 0.17 mM Na_3Cit under boiling conditions. As-synthesized Au nanoparticles were filtered through a 0.22 μm PTFE filter to remove larger particles. The absorbance spectrum of the Au nanoparticle suspension was measured using an Agilent Cary 5000 UV-vis-NIR spectrophotometer (Santa Clara, CA). The absorbance at the peak wavelength of 533 nm was ~1.0, which is equivalent to 0.1 nM based on Beer's law. The Au nanoparticle suspension was concentrated by centrifuging 50 mL of the suspension at 2000 × *g* for 5 min and reducing the volume to 2 mL and 2.5 nM (0.005%, volume content of nanoparticles). To fabricate the binary supraparticles, we mixed the Au and PS nanoparticle suspensions at volumetric ratios (*R*) of 1 : 5, 1 : 7, and 1 : 9 (*i.e.*, 0.025, 0.035, and 0.045% for PS nanoparticle suspension) and further concentrated to 1% volume content of nanoparticles under the above centrifugation condition.

Finally, a 5 μL droplet of the Au and PS nanoparticle mixture was gently deposited onto the superamphiphobic substrate using 10 μL Eppendorf epT.I.P.S. LoRetention Reloads Tips inside a humidity-controlled chamber (Fig. 1B). The relative humidity (RH) was maintained at 40% to control the rate of droplet evaporation. Upon complete drying, the solid-state binary supraparticles were retrieved from the substrates by slightly tilting the substrate. To remove the PS phase from the binary supraparticle and to form a porous structure, we transferred the collected supraparticles into a ceramic cubicle and calcinated in a muffle furnace at 300–500 °C for 4 h.

Characterization

The morphology of the Au nanoparticles was imaged using a JEOL 2100 transmission electron microscope (TEM). For TEM analysis, 10 μL of 0.1 nM Au nanoparticle suspension was deposited onto the copper grid and dried. The analysis was conducted using a field emission gun instrument operating at an accelerating voltage of 200 kV. The diameter was determined using ImageJ.[28] Images of the fabricated superamphiphobic substrate surface and the morphology of the supraparticles were obtained using a JEOL IT500 scanning electron microscope (SEM). Before SEM imaging, the samples were coated with a 5 nm iridium layer using a Leica ACE600 sputter coater. For the supraparticles, two elements (Au and C – representative of PS) were mapped in the SEM images using energy dispersive spectroscopy (EDS). The static contact angle of the water droplet on the superamphiphobic substrate was measured immediately after deposition using a Ramé-Hart Model 250 standard goniometer at room temperature.

SERS detection of environmental contaminants

SERS spectra of six environmental contaminants were obtained using the porous Au supraparticles. An individual porous Au supraparticle was incubated in 100 μL of contaminant-containing solution. The sample was vortex-agitated for several hours unless noted otherwise to allow the contaminants to adsorb to the porous Au supraparticle. After agitation, the porous Au supraparticle was transferred onto dry tissue paper. SERS spectra were obtained using a WITec Alpha500R Raman spectrometer with a 785 nm diode laser (Toptica Photonics, Germany) and a 10× objective lens. The laser power was set to 90 mW. A 300 grooves per mm grating was used, and the spectral center was set to 1500 cm^{-1}. Following microscope focusing, 400 points (20 × 20; $X \times Y$) were measured across a 10 μm × 10 μm area with a 0.1 s integration time per point. The baselines of the collected SERS spectra were subtracted using the shape function in Project Five (v. 5.0; WITec, Germany). The SERS spectra were normalized by the pseudo-peak at 77 cm^{-1} that arises from the plasmon-enhanced electronic Raman scattering (ERS) signal that is cut off by a long-pass filter. It has been reported that the Raman intensity at 77 cm^{-1} reflects the density of the SERS hotspots such that ERS-based SERS normalization reduces spatial variations resulting from heterogenous SERS hotspot distributions and enables improved SERS quantitation.[29,30]

The effects of calcination temperature and the porosity of the Au supraparticle on SERS detection of environmental contaminants were investigated using MGITC as a representative contaminant. Porous Au supraparticles prepared at different calcination temperatures (*i.e.*, 300, 400, and 500 °C) were incubated in 1 μM MGITC solution, and their SERS spectra were obtained. Additionally, porous Au supraparticles with different R_s (*i.e.*, 1 : 5, 1 : 7, and 1 : 9) were used as SERS substrates for MGITC detection. After determining the optimal calcination temperature and porosity, the porous Au supraparticles were used as SERS substrates for the detection of six environmental contaminants: MGITC, RhoB, BZT, ATZ, adenine, and an oligonucleotide gene segment. First, the kinetics of sorption of the environmental contaminants to the porous Au supraparticles were monitored with extended agitation times of 1, 5, 15, 30, 45, 60, 120, and 240 min. After the SERS spectra of the environmental contaminants were obtained, the times for the characteristic Raman peak intensities to plateau were determined. One characteristic peak for each SERS spectrum exhibited the most incredible Raman intensity, and whose position did not overlap with others was chosen for monitoring. For biological analytes (*i.e.*, adenine and gene segment), we introduced 1 mM $MgSO_4$ to quickly attach the molecules to the porous Au supraparticles since Mg^{2+} shields electronegativity between the Au and the analytes.[31,32] The SERS spectra for both were obtained after salt addition and 5 min of agitation.

For sensitivity analysis, solutions with different concentrations of environmental contaminants were prepared and incubated with the porous Au supraparticles. The characteristic Raman peak intensities were plotted against the logarithmic concentrations of the environmental contaminant solutions. Furthermore, multiple contaminant mixtures (*e.g.*, MGITC + RhoB + BZT and adenine (A) + thymine (T) + guanine (G) + cytosine (C)) were incubated with the porous Au supraparticles, and their SERS spectra were obtained to investigate multiplex SERS detection capability. Lastly, the SERS spectra of MGITC in wastewater influent were obtained to investigate the applicability of the porous Au supraparticles as SERS substrates in an environmental matrix.

Results and discussion

Preparation of porous gold supraparticles

Au nanoparticle precursors were synthesized using the seed-mediated method.[33] These Au nanoparticles exhibited a distinct LSPR peak at ~533 nm and have a spherical shape with a mean diameter of ~42.9 ± 6.2 nm ($N = 200$) as determined by ImageJ analysis of collected TEM images (Fig. 2A and B). To generate binary Au/PS supraparticles, we deposited a 5 μL droplet of an Au and PS nanoparticle suspension with a total volume concentration of 1% on a superamphiphobic substrate and then evaporated it under humidity control at room temperature. This superamphiphobic substrate was fabricated by physical and chemical surface treatment of a silicon wafer. The superamphiphobic substrate surface exhibited heterogeneously distributed nanofilaments that were coated with the fluorinated carbon from PFDTS (Fig. 2C). The porous structure of the fluorinated carbon-coated branches provides hydrophobicity to the substrate, thus slightly levitating the mixed droplets of Au and PS above its surface (Fig. 2D). The static contact angle of the droplet (~161.0°) confirmed the hydrophobicity of the substrate and provided a pin-free liquid contact line (Fig. 2E). The contact angle was slightly decreased to 156.7° after 35 min of evaporation and then dramatically decreased to 130.0°, indicating the completion of evaporation (Fig. 2F).

After evaporation, the binary supraparticles were easily transferred onto weigh paper by slightly tilting the substrate. SEM images of supraparticles are shown in Fig. 3A. Hollow dome-shaped supraparticles were observed with ~50 μm thick shells. During evaporation, the concentration of nanoparticles at the air–liquid interface increased, causing shell formation *via* colloidal assembly.[34] Unlike a nanoparticle-filled sphere, the

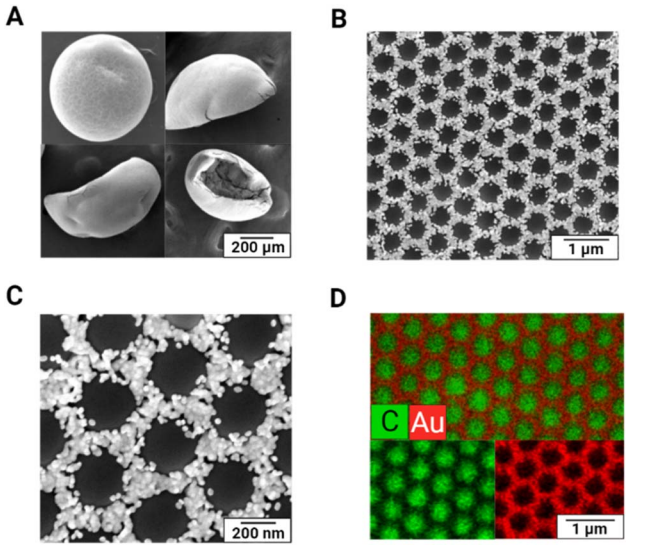

Fig. 3 (A) SEM images of four-side views (top, left, bottom, right, clockwise) of binary supraparticles. (B and C) SEM images of the binary supraparticle surface under low and high magnification. (D) Elemental mapping of the supraparticle surface: overlapping (top) and C, representing PS (bottom left) and Au (bottom right) nanoparticles by energy dispersive spectroscopy (EDS). C and Au are green- and red-colored, respectively.

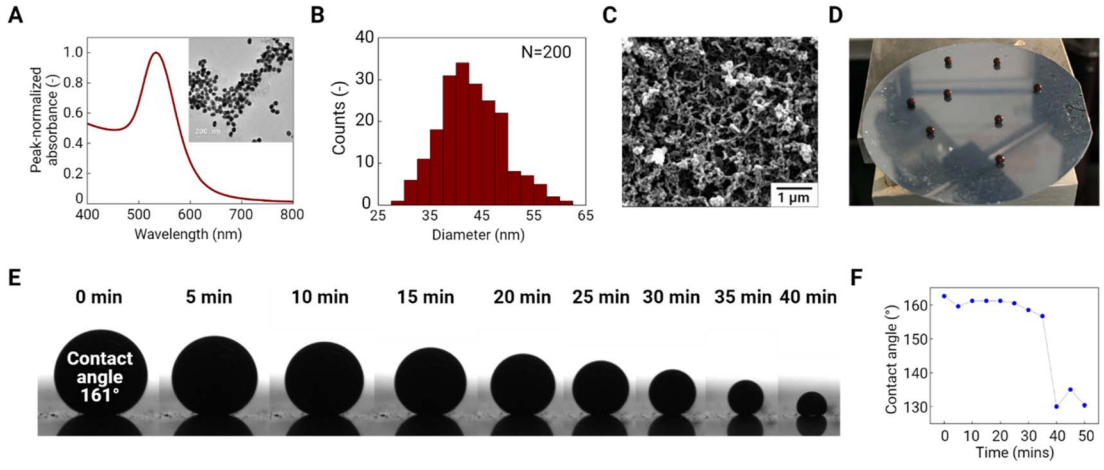

Fig. 2 (A) Absorbance spectrum of the Au nanoparticle suspension. Inset is the TEM image of the Au nanoparticles. (B) Histogram of TEM-determined diameter of the Au nanoparticles ($N = 200$). (C) SEM picture of the superamphiphobic substrate surface. (D) Picture of multiple 5 μL droplets containing a mixture of Au and PS nanoparticles (volume concentration: 1%) on the superamphiphobic substrate. (E and F) Monitoring of the change in the static contact angle with time for a levitated droplet of Au and PS nanoparticles on the superamphiphobic substrate.

hollow shell supraparticles are advantageous for SERS application since they have a shorter diffusion length, allowing more rapid sorption of target molecules to the Au surface.[35] SEM images of the supraparticle surface under different magnifications are shown in Fig. 3B and C. These images clearly show the close-packed array of PS nanoparticles with Au nanoparticle aggregates filling the interstices between PS nanoparticles. Each large-sized PS nanoparticle (600 nm) was surrounded by numerous small-sized Au nanoparticles (43 nm). The colloids were distributed evenly across the surface and this can be attributed to slow evaporation since fast evaporation induced small particles to form an outer shell with large particles enriched at the core.[36] The 50 μm thick shell consisted of multiple layers of Au nanoparticle aggregates that potentially provide a volumetric distribution of SERS hotspots, thus enabling greater SERS enhancement.[37] In addition, the homogeneous distribution of Au and PS nanoparticles was confirmed by elemental mapping of Au and C (Fig. 3D). This image indicates that the two elements do not overlap across the binary supraparticle surface. The EDS spectrum localized over a PS nanoparticle showed a higher mass percent (73.0%) of C compared to Au (25.8%) while one localized over Au nanoparticle aggregates showed 91.8% Au (Fig. S1†). This result implies significantly different spatial distribution of Au and C on the supraparticle surface. We expect that PS phase removal can generate a large porous structure, and the remaining Au-rich nanostructure can provide dense SERS hotspots as a result of LSPR coupling.[24]

Effect of calcination temperature and porosity

To produce a porous Au supraparticle, we removed the PS phase in the binary supraparticle by calcination. We investigated the effect of calcination temperature on the SERS performance of the porous Au supraparticles. SEM images of the porous Au supraparticle surface exhibited different porous structures as a function of calcination temperature (Fig. 4A). At a calcination temperature of 300 °C, PS residuals were observed in the former sites of the PS nanoparticles, indicating incomplete polymer removal. At 400 and 500 °C, the SEM images indicate full removal of PS nanoparticles from the original sites. However, some of the porous structures were filled with melted PS nanoparticles at a calcination temperature of 400 °C. Such differences in the SEM images were reflected in the relative SERS performances of the substrates. SERS spectra of 1 μM MGITC for the Au supraparticles at different calcination temperatures were obtained (Fig. 4B). Obvious SERS spectra of MGITC were found from the Au supraparticles produced at the higher calcination temperatures (400 and 500 °C), while a minimal SERS signal was observed for the Au supraparticles produced at the lower calcination temperature (300 °C). This result demonstrates that larger amounts of PS residues at low calcination temperatures impede close contact of MGITC to the Au surface, thus limiting SERS enhancement. To ensure the complete removal of PS nanoparticles from the supraparticles, we calcinated the supraparticles at 500 °C in the following experiments.

Since a porous structure provides a large surface area and facilitates analyte association with the surface, higher porosities are desirable. We optimized the porosity of the Au supraparticle by adjusting mass ratio R. After the binary supraparticle was formed, the PS phase in the supraparticle was removed by calcination. The space formerly filled by the PS nanoparticles becomes void and acts as the porous structure of the supraparticle. Accordingly, an increased fraction of PS nanoparticles in the mixture is expected to increase the porosity of the Au supraparticle. Three R_s (*i.e.*, 1 : 5, 1 : 7, and 1 : 9) were used to make Au supraparticles with different porosities. SEM images of the porous Au supraparticle surface with different R_s are shown in Fig. 4C. All supraparticle surfaces exhibited clear porous structures, thus indicating that the calcination of the PS nanoparticles succeeded in forming micropores with diameters of several 100 nm, comparable to the diameter of the PS nanoparticles. Three-dimensional Au porous structures were expected to exhibit a strong EM field within their volumes due to effective coupling of the LSPR.[37]

To further analyze the compositional distribution of the supraparticle surface after calcination, elemental maps of the SEM images were obtained using EDS (Fig. 4D). All supraparticle surfaces exhibited high porosity. As R increased, increasingly porous structures were observed. The different concentrations of PS nanoparticles in the droplet provide distinct porous structures following calcination. For an R of 1 : 5, the surface only exhibited distanced holes that reflect the spaces previously filled by PS nanoparticles. For an R of 1 : 9, a majority of the void spaces following PS nanoparticle removal were interconnected and formed a continuous porous structure, which is essential to allow guest molecules to diffuse inside the supraparticle.[25] Interestingly, in the EDS images, carbon was still observed within the porous structure along with Au. This result implies some fraction of PS remained after calcination. We suggest that this residual carbon may increase the affinity of hydrophobic analytes to the supraparticles. The effect of the carbonized PS residues within the porous Au supraparticle on SERS detection of hydrophobic organic contaminants should be further explored.

The effect of Au supraparticle porosity on SERS performance was investigated. The SERS spectra of 1 μM MGITC on the porous Au supraparticles with different R_s are shown in Fig. 4E. Clear SERS spectra of MGITC were obtained from all porous Au supraparticles, thus demonstrating successful SERS detection. To investigate the SERS performance of the Au supraparticles with different porosities, characteristic Raman peak intensities were compared (Fig. 4F). The normalized Raman intensity at 418 cm^{-1} of MGITC for the Au supraparticles increased with an increase in R: 0.334 (± 0.020), 0.343 (± 0.013), and 0.372 (± 0.025) for R_s of 1 : 5, 1 : 7, and 1 : 9. These results show that the introduction of micropores can improve the SERS performance of the porous Au supraparticles.

The strong SERS performance of the porous Au supraparticles can be attributed to the existence of a large porous structure, making it easier for MGITC to diffuse into the Au supraparticles. As a control, a pure Au supraparticle (*i.e.*, assembly from 1% volume concentration of solely Au

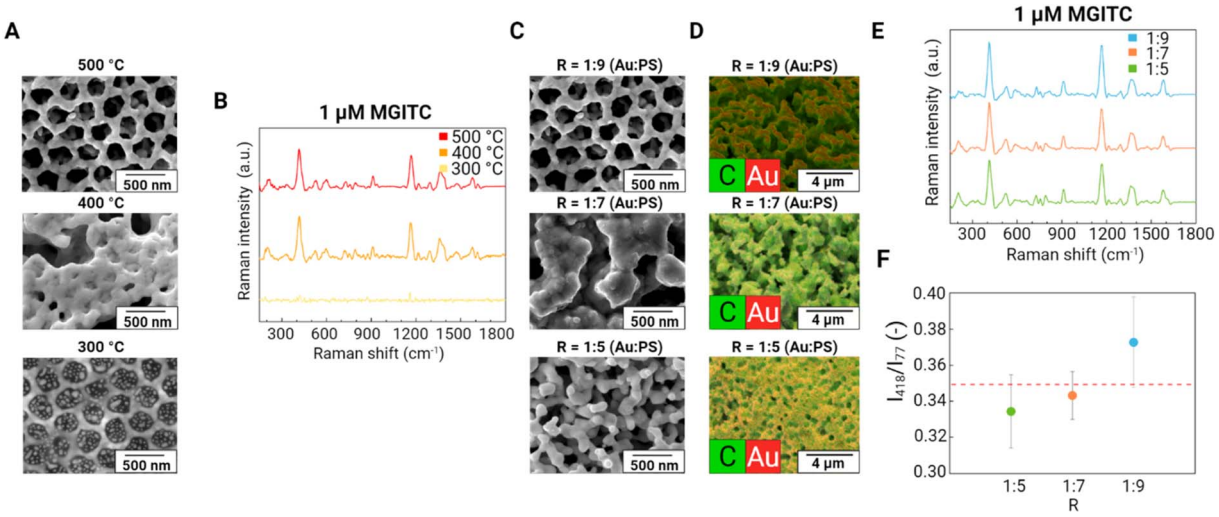

Fig. 4 (A) SEM images of the porous Au supraparticle surface after calcination at different temperatures. (B) Vertically stacked SERS spectra of 1 μM malachite green isothiocyanate (MGITC) were obtained from the porous Au supraparticles at different calcination temperatures. (C and D) SEM and EDS mapping images of the porous Au supraparticle surface with different volumetric ratios (R_s; 1 : 5, 1 : 7, and 1 : 9 from bottom to top) between Au and PS nanoparticles in the droplet for evaporation-induced self-assembly. (E) Vertically stacked SERS spectra of 1 μM MGITC from the porous Au supraparticles with different R_s. (F) Comparison of the characteristic Raman peak intensity at 418 cm^{-1} with different porosities of the Au supraparticles. The symbols and error bars indicate the means and standard deviation of the intensities from the 400 SERS spectra. The red dashed line indicates the same peak intensity with the pure Au supraparticles.

nanoparticle suspension, $R = 1:0$) was evaluated as a SERS substrate. It is worth noting that even a supraparticle made from single primary nanoparticles has naturally emergent nanoscale porosity that arises from the formation of interstitial sites (*i.e.*, the gaps between nanoparticle aggregates).[23] Nonetheless, analyte molecules will primarily associate with the outer shell due to the small size of these interstitial sites. For this reason, it was hypothesized that the microscale porous structure made by PS phase removal in the binary Au/PS supraparticle would increase the accessibility of the guest molecules to inherent SERS hotspots, resulting in better SERS performance than pure Au supraparticles. Interestingly, the normalized Raman intensity of MGITC for the pure Au supraparticle was 0.349 (± 0.011), which is greater than those for the Au supraparticles with the *R*s of 1 : 5 and 1 : 7. This result implies that the porosity should be high enough to exceed the effect of SERS enhancement resulting from the greater number of nanoscale interstitial sites that arise for a pure Au supraparticle. For an *R* of 1 : 9, the porous Au supraparticle exhibited better SERS performance than the pure Au supraparticle. Overall, the *R* of 1 : 9 was chosen as the optimal condition since it exhibited the best SERS performance. The porous Au supraparticle showed excellent SERS performance with a SERS enhancement factor of 1.5×10^5 toward MGITC.

SERS detection of environmental contaminants

Based on the optimal conditions for calcination temperature and the porosity of the Au supraparticle, SERS detection of a range of environmental contaminants was explored. First, two synthetic organic dyes, MGITC and RhoB, were targeted. These chemicals are often considered omnipresent environmental contaminants due to their large-scale production and wide application in textiles, tanning, and printing.[38] Some organic dyes are non-biodegradable such that they are not easily removed by conventional wastewater treatment plants.[39] Next, two organic contaminants, BZT and ATZ, were chosen. BZT is a toxic compound widely used in the pharmaceutical industry and is classified as a priority pollutant by USEPA.[40] ATZ is an example of a herbicide that has been widely used historically.[41] In addition, nucleic acid and its main component, adenine, were targeted. Nucleic acids are of great interest for the characterization of microbial communities and biological function in many environments. For example, integrase-integron class 1 (*int*I1) facilitates the horizon gene transfer among bacteria such that its amount has been used as a proxy to indicate the number of antibiotic resistance genes.[42] In this study, an 86-base length gene segment representative of one region of *int*I1 was targeted (Table S1†).

Due to its porosity, the Au supraparticle can enrich environmental contaminant concentrations from an aqueous solution over a certain contact period. To confirm the sorption of the target analyte (MGITC) in solution to the Au supraparticle, the absorbance spectrum of an aqueous solution was measured using a UV-vis spectrophotometer after 2 h of contact (Fig. S2†). A significant reduction in peak absorbance was found, further indicating the successful sorption of MGITC to the Au supraparticle. As a result, the distinct SERS spectra of environmental contaminants were successfully obtained from the porous Au supraparticles (Fig. 5A). The intense, distinct peaks arising from various vibrational modes are listed in Table S2.† Characteristic peaks for each SERS spectrum that exhibited the greatest Raman intensity and whose position did not overlap with others were chosen as follows: MGITC (418 cm^{-1}, out-of-plane benzene

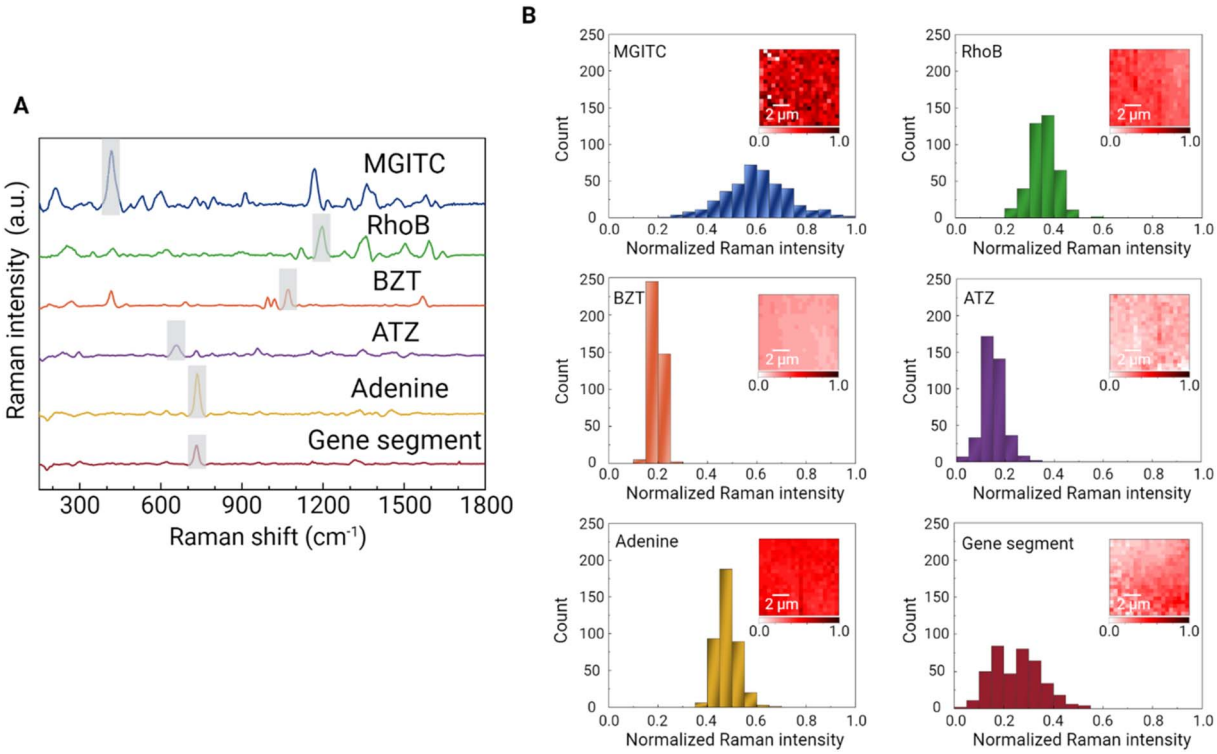

Fig. 5 (A) Vertically stacked SERS spectra of environmental contaminants produced using the porous Au supraparticles: malachite green isothiocyanate (MGITC; 1 μM), rhodamine B (RhoB; 100 μM), benzenethiol (BZT; 10 μM), atrazine (ATZ; 1 mM), adenine (50 μM), and gene segment (50 μM). The dark gray areas indicate the characteristic peaks for each spectrum. (B) Histogram of the normalized Raman intensity of the characteristic peak for a given contaminant across a 10 μm × 10 μm scan area with 20 × 20 ($X \times Y$) points. The insets show the spatial distribution of the Raman intensity across the scan area.

ring deformation[43]), RhoB (1194 cm^{-1}, C–C bridge band stretching[44]), BZT (1068 cm^{-1}, C–C–C bending and C–S stretching[45]), ATZ (655 cm^{-1}, the asymmetric deformation N–C–N/C–N–C and ring breathing[46]), and gene segment (730 cm^{-1}, ring breathing of adenine[47]). Since adenine is one of the main components of the gene segment along with other nucleotides (guanine, thymine, and cytosine), its SERS spectrum exhibited a similar profile to that of the gene segment.[18] Due to these structural similarities, the same characteristic peak was chosen for both analytes. Fig. 5B shows histograms of the characteristic peak intensities for the given contaminants across a 10 μm × 10 μm scan area with 20 × 20 ($X \times Y$) points. For all environmental contaminants, the characteristic Raman peak intensities were normally distributed across the scan area. The coefficients of variation (CV) of the characteristic peak intensities ranged from 8.9 to 37.9%, illustrating the reproducibility of the substrate.

Due to the different affinities of the environmental contaminants to the porous Au supraparticles, sorption kinetics were followed to find the times required to reach equilibrium. The Raman intensities of the characteristic peaks were plotted against the contact time (Fig. S3†). The sorption kinetics for adenine and the gene segment were not obtained since salt-induced association (*i.e.*, electrostatic mediated association at high concentrations of $MgSO_4$) was applied.[31,48] These latter samples were agitated for 5 min after adding the salts to the solution. For other environmental contaminants, the Raman intensities increased over time, characterized by a curvilinear pattern. The results showed that the Raman intensities reached a plateau prior to one hr for RhoB and BZT and two hours for MGITC and ATZ, respectively.

To explore the sensitivity of the porous Au supraparticles as SERS substrates, we incubated all six environmental contaminants with different concentrations with one supraparticle for a predetermined contact period. Following such incubation, the SERS spectra of environmental contaminants from the porous Au supraparticles were obtained. The characteristic Raman peak intensities were plotted against the logarithm of the environmental contaminant concentrations (Fig. 6). The symbols and error bars indicate the means and standard deviations of the Raman peak intensities from 400 SERS spectra. The CVs ranged from 2.7 to 59.8% across six environmental contaminants with different concentrations, indicating the reproducibility of the substrates for detection of the targets. Clear positive linear trends between the two variables were shown with high R-squared values (>0.89) for all six environmental contaminants. These results demonstrate the applicability of the porous Au supraparticles for quantitative SERS analysis. Based on the best-fit linear regression equations and the standard error of the regressions, the limits of detection (LODs) for the six environmental contaminants were determined.[49] MGITC and RhoB had the lowest LODs of 41.0 and 98.4 nM owing to their large Raman cross-sections.[50] MGITC

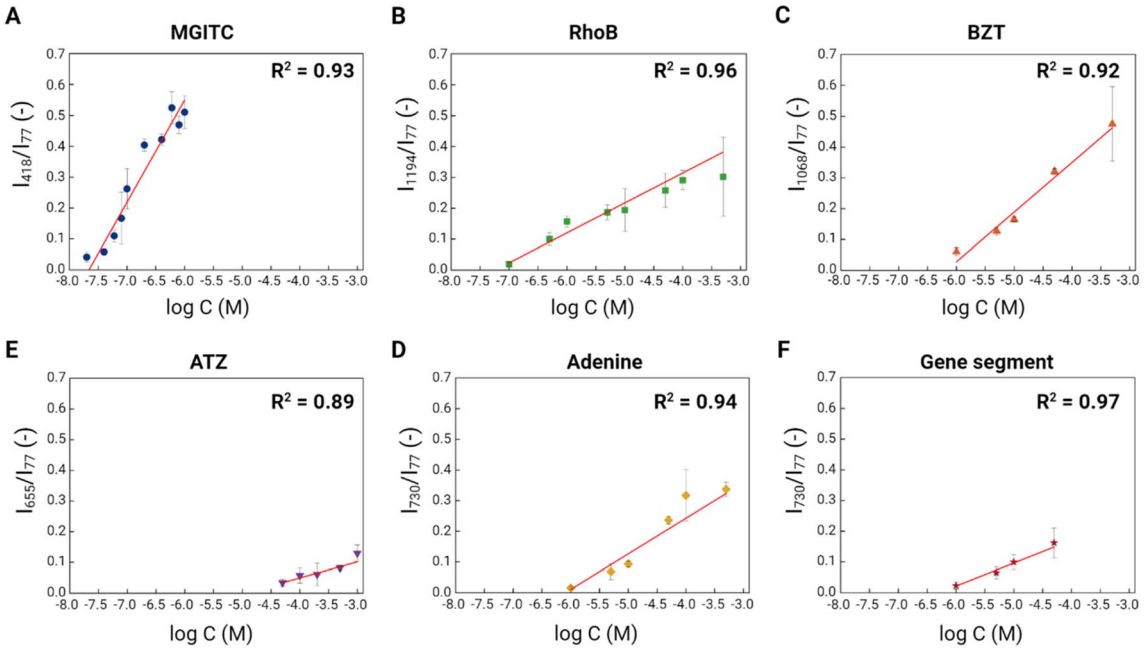

Fig. 6 (A–F) Sensitivity test for six environmental contaminants using the porous Au supraparticles as SERS substrates. Plots of the characteristic Raman peak intensities against the logarithmic concentrations of the environmental contaminants. The symbols and error bars indicate the means and standard deviations of the Raman peak intensities from 400 SERS spectra. The best-fit linear curves were expressed as red-line with the R-squared values.

was more sensitively detectable due to the affinity of its thiol group to the Au surface. The porous Au supraparticle in this study showed slightly better sensitivity for RhoB detection than a previously described Au nanoparticle-based approach.[51] The LODs for BZT and ATZ were 1.8 and 37.7 μM. BZT had a lower detection limit than ATZ, which can be attributed to its thiol group.

ATZ, the most hydrophobic organic contaminant, exhibited the lowest detection sensitivity among the six targets, reflecting its low affinity to the substrate and its small Raman cross-section. We expect that increasing the hydrophobicity of the porous Au supraparticle would enable more sensitive ATZ detection. For example, pyrolysis of the PS phase (*i.e.*, calcination without oxygen in the air) would generate more hydrophobic Au supraparticles. Since the surface affinity of the substrate plays a central role in determining the SERS detection selectivity for the target analyte,[52] surface functionalization can potentially be applied to achieve more sensitive ATZ detection. For example, molecularly imprinted polymer (MIP) functionalized Au nanoparticles were recently used to achieve high selectivity towards ATZ.[53] The gene segment and adenine had comparable LODs of 1.0 and 1.7 μM, which is plausible based on their structural similarities. Unlike other contaminants, the SERS profiles of the adenine and gene segment were quite similar. However, prior studies have successfully discriminated the SERS spectra between different gene sequences through analytical peak ratio comparisons or multivariate data analytics.[18,32] Thus, discriminatory SERS detection of different gene sequences should be possible using the porous Au supraparticles.

Multiplex SERS detection of environmental contaminants

Because the porous Au supraparticle provides a large surface area with dense SERS hotspots, we hypothesized that it could be used to detect multiple environmental contaminants simultaneously. To test such multiplexity, we obtained the SERS spectrum of a mixture containing MGITC, RhoB, and BZT with concentrations of 10 nM, 10 μM, and 5 μM (Fig. 7A). The relative analyte concentrations were adjusted so Raman signals from all three molecules could be detectable. Because every analyte has different cross-sectional Raman signals, if one analyte exhibited significantly higher Raman intensity than others, it could block the Raman signals from the others. The SERS spectrum of the mixture solution exhibited distinct peaks arising from MGITC, RhoB, and BZT (*e.g.*, 915 cm^{-1} from MGTIC; 1197 and 1276 cm^{-1} from RhoB; 998, 1021, and 1069 cm^{-1} from BZT). In addition, multiplex SERS detection of four nucleotides (adenine (A), thymine (T), guanine (G), and cytosine (C)) was also investigated. The SERS spectrum of the mixture solution containing 10 μM of A, T, G, and C was obtained using the porous Au supraparticles (Fig. 7B). The SERS spectrum of the mixture solution exhibited distinct peaks arising from A, T, G, and C (*e.g.*, 730 cm^{-1} from A; 780 cm^{-1} from T; 964 and 1465 cm^{-1} from G; 800 and 1304 cm^{-1} from C). Thus, confirming that the multiplex SERS detection of environmental contaminants was enabled using the porous Au supraparticles.

SERS detection in an environmental matrix

To investigate applicability in real environmental matrices, we tested the porous Au supraparticle in wastewater influent

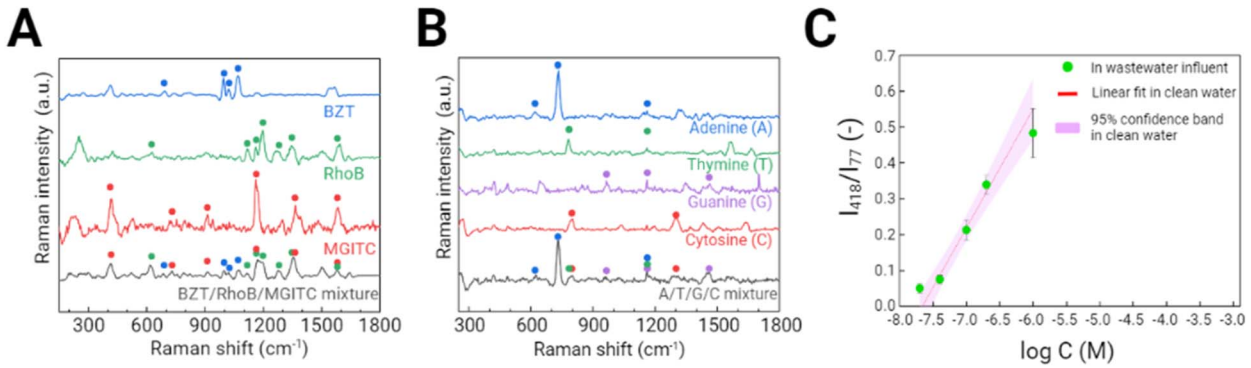

Fig. 7 Multiplex SERS detection of environmental contaminants and SERS detection in environmental matrix. (A) Vertically stacked SERS spectrum of a mixture solution containing 10 nM malachite green isothiocyanate (MGITC), 10 μM rhodamine B (RhoB), and 5 μM benzenethiol (BZT), and their individual spectra. (B) Vertically stacked SERS spectrum of mixture solution containing 10 μM adenine (A), thymine (T), guanine (G), and cytosine (C), and their individual spectra (right). (C) Sensitivity test for MGITC detection in wastewater influent with different concentrations. The symbols and error bars indicate the means and standard deviation of the Raman peak intensity at 418 cm^{-1} from 400 SERS spectra. The best-fit linear curve and a 95% confidence band for MGITC detection in clean water were expressed as a red line and purple area.

containing high amounts of organic matter and high ionic strengths (Table S3†). Different concentrations of MGITC were spiked into wastewater influent and mixed with the Au supraparticles. The result shows the positive linear trend of the characteristic intensity of MGITC at 418 cm^{-1} in wastewater influent against the logarithmic concentration (Fig. 7C). It is apparent that each data point in wastewater influent was well-fitted within the 95% confidence band for the calibration curve obtained for MGITC in nanopure water. This result demonstrates there is limited interference between components in the wastewater influent on the SERS performance of the porous Au supraparticle. In addition, the porous Au supraparticle exhibited stability in wastewater influent throughout the agitation, proving the easy recovery process after analysis.

Conclusions

In this study, facile fabrication of highly porous Au supraparticles was achieved by droplet evaporation of an Au and PS nanoparticle mixture on a superamphiphobic substrate followed by PS removal by calcination. We found that calcination at 500 °C completely removed PS and induced high porosity in the Au supraparticle. As the volumetric ratio between Au and PS nanoparticles in the mixture increased, a higher porous structure was formed in the Au supraparticle and exhibited higher Raman intensity of the adsorbed molecules. A total of six environmental contaminants were mixed with one porous Au supraparticle, respectively, and the distinct SERS spectrum for each target was successfully obtained with great sensitivity. In addition, the porous Au supraparticle was successfully used for multiplex detection of environmental contaminants and exhibited great applicability in an environmental matrix. Interestingly, the pure Au supraparticle also exhibited significant SERS enhancement due to the formation of interstitial gaps between Au nanoparticles. We envision that the micropore formation process *via* the PS phase removal can allow Au supraparticles to capture various-sized guest molecules that will benefit from SERS detection applications. For example, virus and bacteria can be captured into inherent SERS hot-spots resulting from the porous structure.

The low affinity of the porous Au supraparticles to some targets remains a challenge for reliably detecting different environmental contaminants. Expanding the applicability of the porous Au supraparticles as SERS substrates requires further research and engineering efforts, such as surface functionalization of the porous Au supraparticles. Despite this challenge, this study illustrates the promise and strengths of the porous Au supraparticles as SERS substrates for environmental analysis. The supraparticles exhibit dense SERS hot-spots, large surface areas, and stability in an environmental matrix. In addition, it is worth noting that the porous Au supraparticle can serve as a single-supraparticle probe with great sensitivity and convenient handling to minimize the required sample volume.

Conflicts of interest

The authors declare no competing financial interest.

Acknowledgements

Funding for this work was provided through US NSF grants CBET-1705653 and CBET-2029911 to P. V. Laboratory and instrumentation support were provided by NanoEarth a node of the NSF supported NNCI (NSF award number #2025151). Additional support was provided by the Sustainable Nanotechnology Interdisciplinary Graduate Program (VTSuN IGEP) funded by the Virginia Tech Graduate School. Some icons used within the figures were sourced from **https://www.Biorender.com**. We thank Stephen McCartney for helping with the SEM and EDS analyses.

References

1 E. A. Ottesen, J. W. Hong, S. R. Quake and J. R. Leadbetter, *Science*, 2006, **314**, 1464–1467.
2 S. D. Richardson, *Anal. Chem.*, 2008, **80**, 4373–4402.
3 C. Hao, X. Zhao and P. Yang, *TrAC, Trends Anal. Chem.*, 2007, **26**, 569–580.
4 D. Barceló and M. Petrovic, *TrAC, Trends Anal. Chem.*, 2007, **26**, 2–11.
5 S. Rubio and D. Pérez-Bendito, *Anal. Chem.*, 2009, **81**, 4601–4622.
6 A. Ballesteros-Gómez and S. Rubio, *Anal. Chem.*, 2011, **83**, 4579–4613.
7 S. Xu, W. Tang, D. B. Chase, D. L. Sparks and J. F. Rabolt, *ACS Appl. Nano Mater.*, 2018, **1**, 1257–1264.
8 G. Bodelón and I. Pastoriza-Santos, *Front. Chem.*, 2020, **8**, 1–8.
9 S. Jones, A. Pramanik, R. Kanchanapally, B. P. Viraka Nellore, S. Begum, C. Sweet and P. C. Ray, *ACS Sustainable Chem. Eng.*, 2017, **5**, 7175–7187.
10 J. Shan, Y. Zhang, J. Wang, T. Ren, M. Jin and X. Wang, *J. Hazard. Mater.*, 2020, **400**, 123202.
11 K. Y. Hong, C. D. L. de Albuquerque, R. J. Poppi and A. G. Brolo, *Anal. Chim. Acta*, 2017, **982**, 148–155.
12 A. E. Kandjani, Y. M. Sabri, M. Mohammad-Taheri, V. Bansal and S. K. Bhargava, *Environ. Sci. Technol.*, 2015, **49**, 1578–1584.
13 X. Huang, Y. Liu, J. Barr, J. Song, Z. He, Y. Wang, Z. Nie, Y. Xiong and X. Chen, *Nanoscale*, 2018, **10**, 13202–13211.
14 R. A. Halvorson and P. J. Vikesland, *Environ. Sci. Technol.*, 2010, **44**, 7749–7755.
15 P. L. Stiles, J. A. Dieringer, N. C. Shah and R. P. Van Duyne, *Annu. Rev. Anal. Chem.*, 2008, **1**, 601–626.
16 H. Wei, S. M. Hossein Abtahi and P. J. Vikesland, *Environ. Sci.: Nano*, 2015, **2**, 120–135.
17 L. Litti and M. Meneghetti, *Phys. Chem. Chem. Phys.*, 2019, **21**, 15515–15522.
18 S. Kang, I. Kim and P. J. Vikesland, *Anal. Chem.*, 2021, **93**, 9319–9328.
19 S. Yang, X. Dai, B. B. Stogin and T.-S. Wong, *Proc. Natl. Acad. Sci. U. S. A.*, 2016, **113**, 268–273.
20 H. Wei, M. R. Willner, L. C. Marr and P. J. Vikesland, *Analyst*, 2016, **141**, 5159–5169.
21 L. S. Lawson, J. W. Chan and T. Huser, *Nanoscale*, 2014, **6**, 7971–7980.
22 G. B. Braun, S. J. Lee, T. Laurence, N. Fera, L. Fabris, G. C. Bazan, M. Moskovits and N. O. Reich, *J. Phys. Chem. C*, 2009, **113**, 13622–13629.
23 S. Wintzheimer, T. Granath, M. Oppmann, T. Kister, T. Thai, T. Kraus, N. Vogel and K. Mandel, *ACS Nano*, 2018, **12**, 5093–5120.
24 K. Liu, Y. Bai, L. Zhang, Z. Yang, Q. Fan, H. Zheng, Y. Yin and C. Gao, *Nano Lett.*, 2016, **16**, 3675–3681.
25 W. Liu, M. Kappl and H. J. Butt, *ACS Nano*, 2019, **13**, 13949–13956.
26 J. Turkevich, P. C. Stevenson and J. Hillier, *Discuss. Faraday Soc.*, 1951, **11**, 55–75.
27 G. FRENS, *Nat. Phys. Sci.*, 1973, **241**, 20–22.
28 S. J. Abramoff, M. D. Magalhães and P. J. Ram, *Biophotonics Int.*, 2004, **11**, 36–42.
29 W. Nam, Y. Zhao, J. Song, S. Ali Safiabadi Tali, S. Kang, W. Zhu, H. J. Lezec, A. Agrawal, P. J. Vikesland and W. Zhou, *J. Phys. Chem. Lett.*, 2020, **11**, 9543–9551.
30 H. Wei, W. Leng, J. Song, M. R. Willner, L. C. Marr, W. Zhou and P. J. Vikesland, *Anal. Chem.*, 2018, **90**, 3227–3237.
31 S. Dick and S. E. J. Bell, *Faraday Discuss.*, 2017, **205**, 517–536.
32 L. J. Xu, Z. C. Lei, J. Li, C. Zong, C. J. Yang and B. Ren, *J. Am. Chem. Soc.*, 2015, **137**, 5149–5154.
33 K. R. Brown, D. G. Walter and M. J. Natan, *Chem. Mater.*, 2000, **12**, 306–313.
34 W. Shim, C. S. Moon, H. Kim, H. S. Kim, H. Zhang, S. K. Kang, P. S. Lee and S. Wooh, *Crystals*, 2021, **11**, 79.
35 Y. Wang, F. Su, J. Y. Lee and X. S. Zhao, *Chem. Mater.*, 2006, **18**, 1347–1353.
36 W. Liu, J. Midya, M. Kappl, H.-J. Butt and A. Nikoubashman, *ACS Nano*, 2019, **13**, 4972–4979.
37 X. Zhang, X. Zhang, C. Luo, Z. Liu, Y. Chen, S. Dong, C. Jiang, S. Yang, F. Wang and X. Xiao, *Small*, 2019, **15**, 1–8.
38 A. Tkaczyk, K. Mitrowska and A. Posyniak, *Sci. Total Environ.*, 2020, **717**, 137222.
39 H. Ali, *Water, Air, Soil Pollut.*, 2010, **213**, 251–273.
40 Z. Li, Y. Wu, Y. Shen and B. Gu, *ACS Omega*, 2020, **5**, 10808–10814.
41 M. Graymore, F. Stagnitti and G. Allinson, *Environ. Int.*, 2001, **26**, 483–495.
42 M. R. Gillings, W. H. Gaze, A. Pruden, K. Smalla, J. M. Tiedje and Y. G. Zhu, *ISME J.*, 2015, **9**, 1269–1279.
43 A. Kamińska, I. Dzięcielewski, J. L. Weyher, J. Waluk, S. Gawinkowski, V. Sashuk, M. Fiałkowski, M. Sawicka, T. Suski, S. Porowski and R. Hołyst, *J. Mater. Chem.*, 2011, **21**, 8662.
44 S. Aghajani, A. Accardo and M. Tichem, *ACS Appl. Nano Mater.*, 2020, **3**, 5665–5675.
45 F. Madzharova, Z. Heiner and J. Kneipp, *J. Phys. Chem. C*, 2020, **124**, 6233–6241.
46 S. Bonora, E. Benassi, A. Maris, V. Tugnoli, S. Ottani and M. Di Foggia, *J. Mol. Struct.*, 2013, **1040**, 139–148.
47 L. Guerrini, Ž. Krpetić, D. van Lierop, R. A. Alvarez-Puebla and D. Graham, *Angew. Chem.*, 2015, **127**, 1160–1164.
48 S. E. J. Bell and N. M. S. Sirimuthu, *J. Am. Chem. Soc.*, 2006, **128**, 15580–15581.
49 A. Shrivastava and V. Gupta, *Chron. Young Sci.*, 2011, **2**, 21.
50 N. P. W. Pieczonka and R. F. Aroca, *Chem. Soc. Rev.*, 2008, **37**, 946.
51 Y. Sun, W. Li, L. Zhao, F. Li, Y. Xie, W. Yao, W. Liu and Z. Lin, *Food Chem.*, 2021, **357**, 129741.
52 J. C. S. Costa, R. A. Ando, P. H. C. Camargo and P. Corio, *J. Phys. Chem. C*, 2011, **115**, 4184–4190.
53 B. Zhao, S. Feng, Y. Hu, S. Wang and X. Lu, *Food Chem.*, 2019, **276**, 366–375.